

# RSC Advances



This is an *Accepted Manuscript*, which has been through the Royal Society of Chemistry peer review process and has been accepted for publication.

*Accepted Manuscripts* are published online shortly after acceptance, before technical editing, formatting and proof reading. Using this free service, authors can make their results available to the community, in citable form, before we publish the edited article. This *Accepted Manuscript* will be replaced by the edited, formatted and paginated article as soon as this is available.

You can find more information about *Accepted Manuscripts* in the [Information for Authors](#).

Please note that technical editing may introduce minor changes to the text and/or graphics, which may alter content. The journal's standard [Terms & Conditions](#) and the [Ethical guidelines](#) still apply. In no event shall the Royal Society of Chemistry be held responsible for any errors or omissions in this *Accepted Manuscript* or any consequences arising from the use of any information it contains.

## ARTICLE

# Photoelectrochemical Response and Electronic Structure Analysis of Mono-Dispersed Cuboid-Shaped $\text{Bi}_2\text{Fe}_4\text{O}_9$ Crystals with Near-Infrared Absorption

Cite this: DOI: 10.1039/x0xx00000x

Yangyang Zhang, Yiping Guo\*, Huanan Duan, Hua Li, Lei Yang, Pei Wang, Chongyang Sun, Biyi Xu, Hezhou Liu\* ,

Received 00th January 2012,  
Accepted 00th January 2012

DOI: 10.1039/x0xx00000x

[www.rsc.org/](http://www.rsc.org/)

An n-type mono-dispersed cuboid-shaped  $\text{Bi}_2\text{Fe}_4\text{O}_9$  semiconductor is synthesized via a hydrothermal method in concentrated NaOH solution. It is demonstrated that  $\text{Bi}_2\text{Fe}_4\text{O}_9$  phase is formed by the reaction of  $\text{Bi}_{25}\text{FeO}_{40}$  crystal and amorphous  $\text{Fe}(\text{OH})_3$ . A doctor-blade technique is employed to determine the orientation of  $\text{Bi}_2\text{Fe}_4\text{O}_9$  cuboids. It is found that the cuboids are preferentially grown along [001] direction with side facets (110) and  $(\bar{1}10)$  parallel to it. The UV-Visible-Near infrared absorption spectrum shows that besides two broad absorption edges in visible spectrum region, remarkable near-infrared absorption is also observed, indicating  $\text{Bi}_2\text{Fe}_4\text{O}_9$  is a promising semiconductor capable of utilizing all solar band energy. Hence, steady and distinct photocurrents are measured to be  $0.35 \mu\text{A cm}^{-2}$ ,  $7 \mu\text{A cm}^{-2}$  and  $33 \mu\text{A cm}^{-2}$  under near-infrared irradiation, visible-light and simulated sunlight, respectively. First principle calculation is used to reveal the electronic structure of  $\text{Bi}_2\text{Fe}_4\text{O}_9$  and the derived band gap is 1.23 eV, which agrees well with our experimental value of 1.29 eV. The calculation results also show that  $\text{Bi}_2\text{Fe}_4\text{O}_9$  is an indirect bandgap semiconductor which is contrary to previous results. Besides, the extra absorption peak at around 700 nm in the UV-Visible-Near infrared spectrum should be attributed to the intervalence charge transfer induced by unevenly distributed  $[\text{FeO}_6]^{9-}$  octahedrons and  $[\text{FeO}_4]^{5-}$  tetrahedrons rather than the previously reported d-d transition which is both spin and laporte forbidden. Our work provides deep insights into the nature of the band structure of  $\text{Bi}_2\text{Fe}_4\text{O}_9$ , and will facilitate the design of composite photoanode that can response to near-infrared light.

## Introduction

Conventional n-type metal oxides such as  $\text{TiO}_2$ ,  $\text{WO}_3$  and  $\text{ZnO}$  for applications in photoanodes and photocatalysts have been intensively studied.<sup>1-3</sup> However, they can merely respond to ultraviolet (UV) light owing to their wide band gaps (typically  $\sim 3.2$  eV) and thus the solar energy utilization is insufficient. Hence, narrow bandgap metal oxides capable of capturing a substantial part of visible light are receiving more and more attention. For example, some metal oxides, such as  $\text{Bi}_2\text{WO}_6$  which is reported to be able to harvest near-infrared (NIR) irradiation and organometal halide perovskites (i.e.  $\text{CH}_3\text{NH}_3\text{PbI}_3$ ) which possess high molar absorption coefficient in all visible light range are now hot topics in photovoltaic applications.<sup>4,5</sup>

Multiferroic  $\text{BiFeO}_3$  with a band gap of  $\sim 2.2$ - $2.8$  eV has attracted a great deal of attention for its potential applications in resistive memory and solar cells.<sup>6-8</sup> As another typical bismuth ferrite,  $\text{Bi}_2\text{Fe}_4\text{O}_9$  (BFO) with a previously evaluated narrow band gap of  $\sim 2.0$  eV is also of interest. Most studies to date have focused on using BFO as powder-type photocatalysts for decomposition of organic compounds or as semiconductor gas sensors rather than using BFO as

a photoanode in a water photoelectrolysis cell and as sensors in NIR related areas.<sup>9-12</sup>

BFO can be obtained via traditional solid-state reaction method, chemical co-precipitation route, sol-gel method, molten-salt technique and hydrothermal process.<sup>12-16</sup> However, pure BFO is difficult to prepare because the kinetics of phase formation in the  $\text{Bi}_2\text{O}_3$ - $\text{Fe}_2\text{O}_3$  pseudo-binary system can easily lead to the coexistence of compounds such as  $\text{BiFeO}_3$ , BFO and  $\text{Bi}_{25}\text{FeO}_{40}$ .<sup>17</sup> Among all the methods that have been developed, hydrothermal process is a controllable, low temperature, facile and cost effective method to realize large scale production of pure orthorhombic BFO with regular shapes including nanosheets, nanoplates and microcubes.<sup>18</sup> To date, the synthesis of mono-dispersed BFO crystal with regular shape and uniform size via hydrothermal method has not been reported, and the chemical reactions during the synthesis of BFO crystals remain unclear.

To the best of our knowledge, a large majority of single-phased metal oxide semiconductors usually have only one absorption edge in visible light range. However, BFO exhibits two distinct absorption edges in visible light range, one is from 610 nm and the other is from

850 nm.<sup>9, 12, 19</sup> To interpret the origin of an extra absorption edge observed at 850 nm, Sun and co-workers carried out the first principle calculation and they proposed a middle band ( $E_m$ ) that consisted of  $Fe e_g(O)/Fe t_{2g}(T)$ . BFO was thus defined as a multiband semiconductor with two band gaps (2.05 eV and 1.53 eV) and the extra absorption edge was ascribed to the d-d transition between  $E_m$  and the bottom of the conduction band composed of  $Fe t_{2g}(O)/Fe e_g(T)$ .<sup>12, 19</sup> Besides, a symmetric density of states (DOS) for BFO which is spin polarized is also proposed. On the contrary, Pchelkina et al. derived an asymmetric DOS in BFO and a single bandgap varied from 0.97 eV to 1.28 eV based on their *Ab initio* investigation.<sup>20</sup> Therefore, whether BFO belongs to a multiband semiconductor or not are still quite elusive and the conclusion that d-d transition results in the extra absorption edge remains controversial as well. It is known that semiconductors can be divided into two categories, namely direct bandgap semiconductor and indirect semiconductor, depending on the feature of their interband transitions.<sup>21</sup> On the basis of optical spectrum, Tauc's relation is a frequently used method to determine the interband transition type.<sup>22</sup> However, it is not sufficient to tell the feature of the interband transition only through this relationship. First principle calculations have successfully predicted the interband transition feature of many semiconductors including silicon (Si), germanium (Ge), gallium arsenide (GaAs), zinc sulfide (ZnS),  $BiFeO_3$  and so on.<sup>23, 24</sup> BFO was used to be regarded as a direct band gap semiconductor with a narrow band gap of  $\sim 2.0$  eV according to the analysis of its UV-Vis spectrum.<sup>12</sup> However, there is no theoretical calculations on determining its interband transition type up to now.

In this study, mono-dispersed BFO cuboids were successfully synthesized via a hydrothermal method. The growth mechanism, the origin of the extra absorption edge, the interband transition feature and the photoelectrochemical response of the cuboid-shaped BFO were studied. An interesting NIR response was first observed and analyzed in the BFO crystals.

## Experimental

**Synthesis of BFO cuboids:** All chemicals used in the synthesis of BFO cuboids are of analytical grade purchased from Sinopharm Chemical Reagent Co., Ltd. The precursor suspensions were prepared by using bismuth nitrate ( $Bi(NO_3)_3 \cdot 5H_2O$ ), ferric nitrate ( $Fe(NO_3)_3 \cdot 9H_2O$ ) and sodium hydroxide (NaOH) as the starting materials. Briefly, 3 mmol  $Bi(NO_3)_3 \cdot 5H_2O$  was added into 40 ml deionized (DI) water under constant stirring for 1 h to give a homogeneous milk-white suspension, which is resulted from the hydrolysis of bismuth nitrate. 6 mmol  $Fe(NO_3)_3 \cdot 9H_2O$  was then added to the above suspension and stirred for another 1 h. Subsequently, 0.75 mol NaOH was dropped in slowly to precipitate  $Bi^{3+}$  and  $Fe^{3+}$  and the molar concentration of NaOH is 18.75 M. The as-obtained dark brown mixture was transferred into a 50 ml Teflon-lined stainless-steel autoclave to 80% of its total volume. The autoclave was held at 180 °C for different time (0 h, 0.5 h, 1 h, 2 h, 6 h, 24 h) and then cooled down to ambient temperature naturally. The final products, denoted as S-0h, S-0.5h, S-1h, S-2h, S-6h and S-24h hereafter, were obtained by washing with DI water for several times to remove any possible diffluent impurities followed by drying at 60 °C for 5 h.

**Characterization:** Morphologies of the products were observed with a field emission scanning electron microscope (FEI Sirion 200 SEM) operated at 10 kV. Phase purity was confirmed by powder XRD analysis (Rigaku D/MAX2550vl/84,  $Cu K\alpha$  radiation) from 10° to 70° (2 $\theta$ ) at a scan rate of 4 °/min under 35 kV and 200 mA. Diffuse-reflectance spectroscopy of the sample S-24h was measured by UV-Vis-NIR spectrometer (PerkinElmer 750S) between 200-1500 nm with analytical  $BaSO_4$  powder as the baseline correction material. X-

ray photoelectron spectrum (XPS) was collected on a Kratos Axis Ultra DLD using  $Mg K\alpha$  radiation as the X-ray source.

**Preparation of doctor-blade BFO (DB-BFO):** A doctor-blade technique was used to determine the orientation of cuboid shaped BFO crystals because a substantial part of BFO cuboids were likely to lie down to lower their barycenter upon scraping and finally resulted in an oriented BFO film. In our work, a mixture of 3 g S-24h and 6 ml 5 wt.% polyvinyl alcohol (PVA, analytical reagent) aqueous solution was deposited onto a cleaned glass slide with a doctor-blade coating method followed by calcination at 500 °C for 3 h to remove PVA.

**Photoelectrochemical measurement:** For photoelectrochemical measurements, BFO film electrode with a thickness up to  $\sim 20$   $\mu m$  was prepared on fluorine doped tin oxide (FTO) glass using the doctor-blade method. A strip of copper foil was connected to the conductive side of FTO glass using conductive tape to create an ohmic contact. Then the whole device was sealed with insulating epoxy resin to control the exposed area of BFO film to be 1 cm $\times$ 1 cm. The photoelectrochemical performance of cuboid-shaped BFO film electrodes were performed in a three electrode setup in a 0.1 M potassium phosphate ( $K_3PO_4$ ) solution (pH=7) with platinum (Pt) electrode acting as the counter electrode and saturated calomel electrode (SCE) in saturated potassium chloride (KCl) as the reference electrode. The working electrode was irradiated using a 350 W Xe arc lamp (XQ-350) either with or without a cutoff filter ( $\lambda > 420$  nm or  $\lambda > 780$  nm) from the back of the FTO glass. All time-dependent photocurrents with chopped illumination were carried out under a constant bias of +0.7 V (vs. SCE) within 400 s.

**Electronic structure calculation:** First-principle calculation was performed on the Castep module of Material Studio using the all-electron Blöchl's projector augmented wave (PAW) method, within the PBE version of the generalized gradient approximation (GGA) to depict the exchange correlation functional.<sup>25, 26</sup> Accounting for the antiferromagnetic nature of BFO and the strong electronic correlations on the Fe sites, spin polarized calculation and LDA+U approximation were introduced.<sup>27, 28</sup> The cutoff energy of plane wave was set as 450 eV. The k-points sampling in Brillouin zone were carried out using Monkhorst-Pack scheme (Fig. S1).<sup>29</sup>

## Results and Discussion

The purity and phase structure of the as-prepared samples were examined by XRD patterns. As shown in Fig. 1. It is evident that the XRD patterns of S-0h and S-0.5h can be fully indexed to the cubic structure of  $Bi_{25}FeO_{40}$  (space group:  $I23$ , JCPDS 46-0416), whose chemical formula actually is  $Bi_{12}(Bi_{0.5}Fe_{0.5})O_{19}$ .<sup>30</sup> All diffraction peaks in the XRD patterns for S-2h, S-6h and S-24h samples match well with the single-phase orthorhombic BFO (space group:  $Pbam$ , JCPDS 25-0090). Fig. 2 shows the morphology and fine structure of the BFO crystals synthesized at 180 °C for various time. It can be observed from Fig. 2(a) that S-0h is primarily composed of a large quantity of randomly distributed  $Bi_{25}FeO_{40}$  nanoparticles with diameters of about 20 nm. The nanoparticles then begin to assemble into roughly cuboid-like aggregations of  $Bi_{25}FeO_{40}$  (Fig. 2b), which are probably embryos of the well-crystallized BFO cuboids. After the hydrothermal time reaches to 1h, cuboid-shaped BFO crystals with plenty of residual  $Bi_{25}FeO_{40}$  nanoparticles adhered to their surfaces come into being (Fig. 2c). The XRD pattern of S-1h in Fig. 1 also suggests the coexistence of BFO and  $Bi_{25}FeO_{40}$  crystals, which is consistent to the corresponding SEM image (Fig. 2c). Single-phase BFO cuboids can be obtained after 2 h's reaction, but massive large

porous defects are randomly distributed on their surfaces (Fig. 2d and 2e). By further increasing the reaction time to 24 h, perfect mono-dispersed cuboid-shaped BFO crystals (Fig. 2f) with length of 2.8–3.2  $\mu\text{m}$  and transverse size of 0.9–1.1  $\mu\text{m}$  are finally obtained. It is worth noting that the tiny fragments appeared in Fig. 2f are also BFO rather than impurities according to the XRD pattern of S-24h in Fig. 1 and the energy dispersive spectrum (EDS) results in Fig. S2. These tiny fragments should be generated by the combination of fierce thermal motion and longtime corrosion of concentrated NaOH solution which as well results in crystal size reduction. As introduced in the experimental part, the mole ratio of Bi and Fe in raw materials is 1:2, while the value of the  $\text{Bi}_{25}\text{FeO}_{40}$  crystals appeared in S-0h and S-0.5h

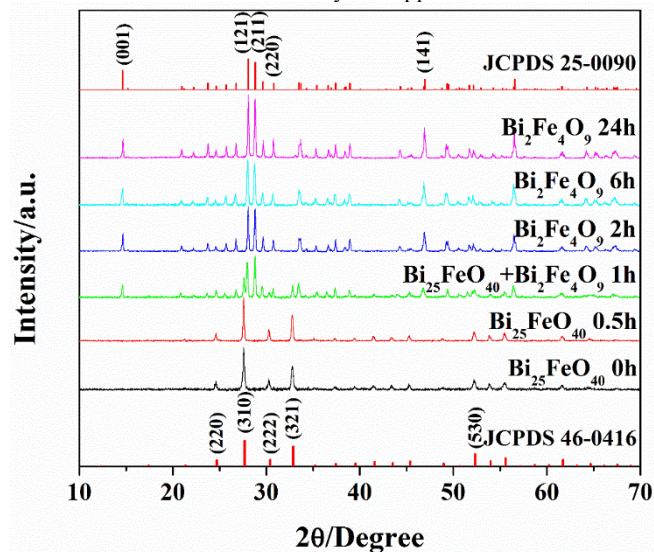


**Fig. 1.** X-ray diffraction patterns of the hydrothermal products synthesized at 180 °C for (a) 0, (b) 0.5, (c) 1, (d) 2, (e) 6 and (f) 24 h. The vertical lines at the bottom and the top correspond to the standard XRD patterns of cubic  $\text{Bi}_{25}\text{FeO}_{40}$  (JCPDS 46-0416) and orthorhombic  $\text{Bi}_2\text{Fe}_4\text{O}_9$  (JCPDS 25-0090), respectively.

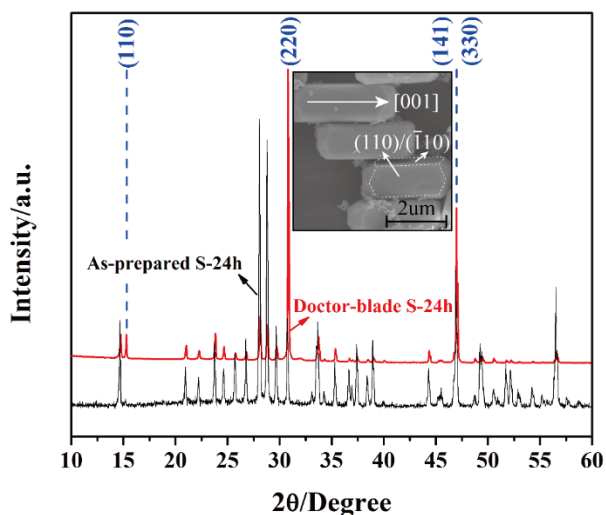


**Fig. 3** XRD patterns of the BFO cuboids prepared at 180 °C for 24 h and its corresponding doctor-blade sample (DB-BFO). The inset shows the SEM image of the doctor blade sample, in which the preferential growth direction and main crystal induces are labeled.

By taking advantage of the large dimension of the BFO cuboid, its orientation was determined using a DB-BFO sample assisted by XRD

is merely 25:1. Therefore, there must be other iron rich amorphous substances exist in S-0h and S-0.5h, which probably iron hydroxide ( $\text{Fe}(\text{OH})_3$ ), because a light brown sol (Fig. S3) exhibiting Tyndall effect is formed after dispersing the iron rich amorphous precipitate in DI water. In addition, compared with the content of Bi in the dried brown sol, far more abundant Fe is found according to the EDS results (Fig. S4), which further demonstrates that the sol is primarily composed of iron hydroxide. As a result, the time-dependent experiments suggest that BFO crystal nucleuses are originated from a chemical reaction involving  $\text{Bi}_{25}\text{FeO}_{40}$  and  $\text{Fe}(\text{OH})_3$  instead of a phase transformation process.

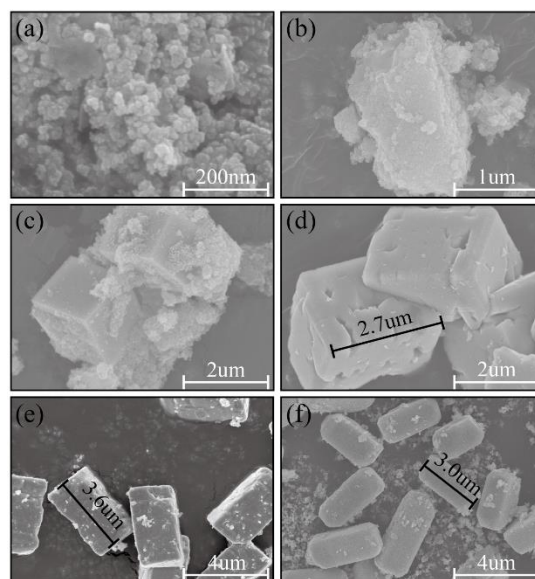
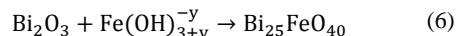
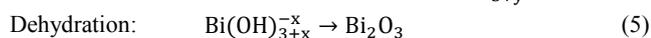
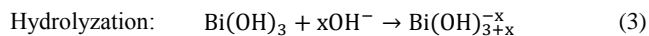
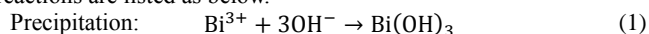


**Fig. 2.** FE-SEM images of the hydrothermal products synthesized at 180 °C for (a) 0, (b) 0.5, (c) 1, (d) 2, (e) 6 and (f) 24 h

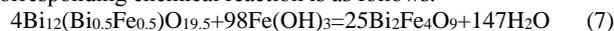
rather than via a typical TEM approach. Fig. 3 presents the XRD patterns of the as-prepared S-24h and its doctor-blade sample (DB-BFO). In contrast with the XRD pattern of S-24h, the relative intensities of the (110), (220) and (330) peaks to those of other peaks are enhanced significantly for the DB-BFO sample, suggesting more (110), (220) and (330) facets meet Bragg's law as a result of the alignment of BFO cuboids after scraping (inset of Fig. 3, Fig. S5). Consequently, the rectangular crystal facets, as shown in the inset of Fig. 3, should be either (110) or  $(\bar{1}10)$ . The preferential growth direction of BFO cuboid should be [001], zone-axis of (110) and  $(\bar{1}10)$  facets, which agrees well with the TEM results reported previously.<sup>12, 15, 18</sup>

The phase and morphology evolution process during the formation of cuboid-shaped BFO were illustrated in Fig. 4. Initially,  $\text{Bi}(\text{NO}_3)_3$  and  $\text{Fe}(\text{NO}_3)_3$  hydrolyze into several complicated water insoluble basic salt precipitation in DI water and make the pH value decrease. Upon the addition of NaOH to the above mixture, both  $\text{Bi}(\text{OH})_3$  and  $\text{Fe}(\text{OH})_3$  sediments spring up immediately and they will further react with  $\text{OH}^-$  to form a dense precursor composed of  $\text{Bi}(\text{OH})_{3+x}^-$  and  $\text{Fe}(\text{OH})_{3+y}^-$ . The solubility product constant of  $\text{Bi}(\text{OH})_3$  is  $4 \times 10^{-31}$  which is a few orders of magnitude larger than that of  $\text{Fe}(\text{OH})_3$  ( $4 \times 10^{-38}$ ).<sup>31</sup> Therefore, the hydrolysis of  $\text{Bi}(\text{OH})_3$  is more significant than that of  $\text{Fe}(\text{OH})_3$ , which will lead to a higher concentration of  $\text{Bi}(\text{OH})_{3+x}^-$  compared to that of  $\text{Fe}(\text{OH})_{3+y}^-$  in the precursor.

Subsequently, monoclinic  $\text{Bi}_2\text{O}_3$  served as an intermediate product, which is confirmed by a self-designed experiment as presented in Fig. S6, is formed at first during the dehydration stage owing to the higher concentration of  $\text{Bi}(\text{OH})_{3+x}^-$ . As illustrated in Fig. 4(a), the  $\text{Bi}_{25}\text{FeO}_{40}$  crystals presented in S-0h should be attributed to the following reaction between  $\text{Bi}_2\text{O}_3$  and  $\text{Fe}(\text{OH})_{3+y}^-$ . The main possible chemical reactions are listed as below.<sup>32, 33</sup>



As the reaction proceeding, the cuboid-like aggregation composed of  $\text{Bi}_{25}\text{FeO}_{40}$  and  $\text{Fe}(\text{OH})_3$  particles appears (Fig. 4b). When the compactness of the aggregation reaches a certain value, BFO nucleus start to generate due to the reaction between  $\text{Bi}_{25}\text{FeO}_{40}$  crystals and its surrounding residual  $\text{Fe}(\text{OH})_3$  (Fig. 4c). The recrystallization reaction will not be terminated until all amorphous  $\text{Fe}(\text{OH})_3$  are consumed. The corresponding chemical reaction is as follows.



Previous studies had shown that the dominant facets of BFO crystals were (001), (110) and  $(\bar{1}10)$ ,<sup>34</sup> which was also confirmed in

our study. According to the Bravais law, the growth rate of (110)/ $(\bar{1}10)$  facets should be higher than that of (001) facet owing to their smaller interplanar spacing and lattice point density (Fig. 4d). Hence, BFO intrinsically prefers to grow along [110] or  $[\bar{1}10]$  directions to form nano-plate which has been achieved at low NaOH concentrations previously.<sup>18</sup> However, in our experiment, BFO only grows along [001] direction to form cuboids and this abnormal growth habit should result from the high NaOH concentration (18.75 M). Products prepared with lower NaOH concentrations (12.5 M, 6.25 M, 2.5 M, 1 M, 0.5 M and 0.25 M) were characterized by SEM and XRD, as shown in Fig. S7 and Fig. S8. BFO cannot be formed at NaOH concentrations less than 2.5 M and the aspect ratio of BFO decreases with the reduction of NaOH concentration which confirms the role of NaOH concentration. It is suggested that  $\text{OH}^-$  ions are favorable to adsorb onto the (110)/ $(\bar{1}10)$  facets of an oxide crystal which is bound to prevent the  $\text{Fe}(\text{OH})_3$  particles from approaching and thus modifies the intrinsic growth habit, as shown in Fig. 4d.<sup>35, 36</sup> The “blocking effect” of  $\text{OH}^-$  is enhanced with the increase of NaOH concentration. Therefore, the growth rates of (110)/ $(\bar{1}10)$  facets will be reduced with the addition of NaOH while the growth rate of (001) is scarcely influenced, which eventually leads to BFO cuboids with orientation of [001] (Fig. 4e).

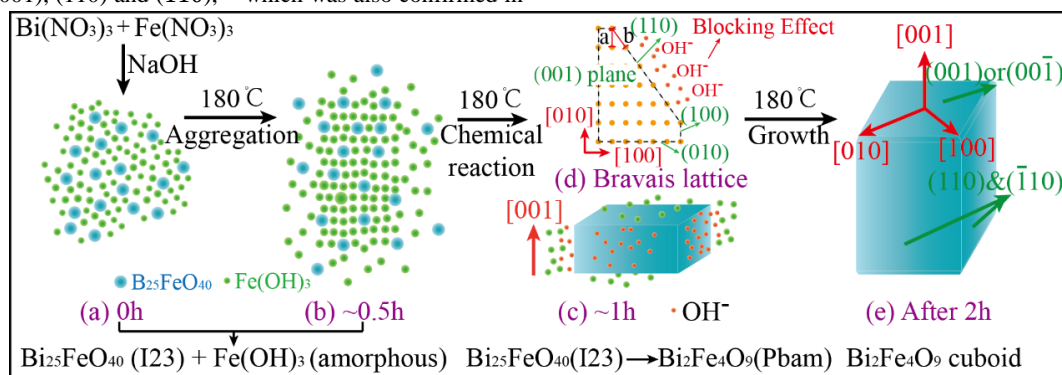


Fig. 4 Schematic diagram of the morphology and phase evolution process of BFO cuboids.

From the magnified FE-SEM images centered by one corner of the BFO cuboid, one can see that some extra small facets occupy the position of some edges, as displayed in Fig. 5. Obviously, two small facets, which are labelled as 1 and 2 in both Fig. 5(a) and (b) appear at the edges of (001) surface while no facets are discovered at the edges that are perpendicular to (001), such as edge 4 in Fig. 5(a), (b).

It is also noticeable that the sharp edge 4 and vertex 3 of S-2h change into blunt ones due to the corrosion of alkali and violent thermal motion. For better understanding of the fine structure of BFO cuboid, a schematic of an individual BFO cuboid with all existing surfaces is presented in Fig. 5(c).

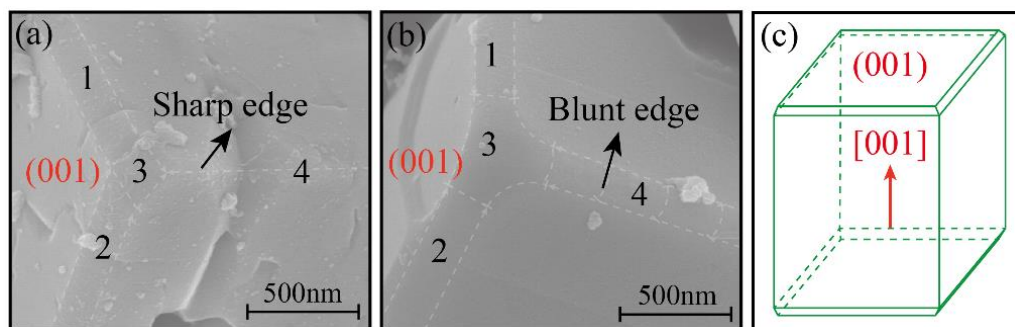
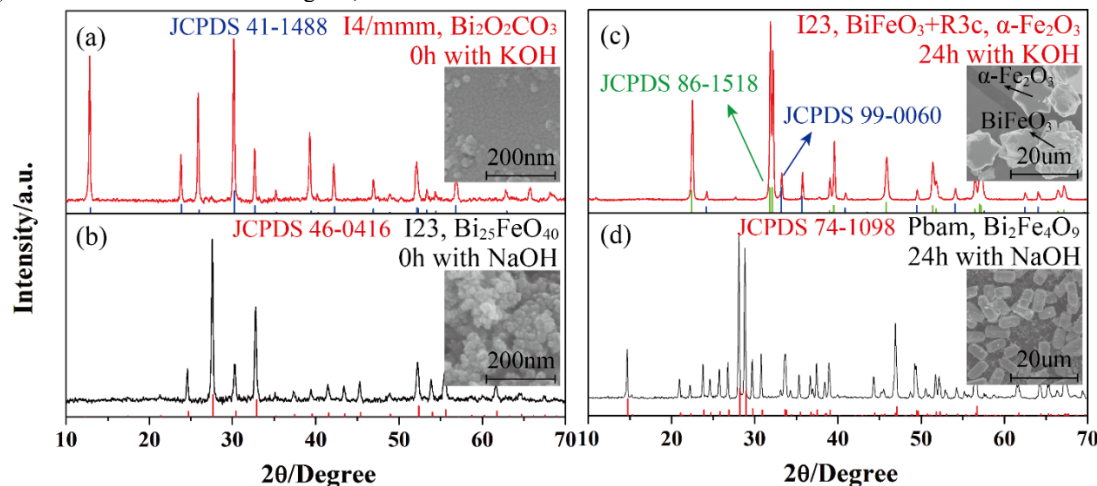


Fig. 5. SEM images of small facets on the edges of S-2h (a) and S-24h (b). Schematic (c) outlines the detailed profile of an individual BFO cuboid.

The influence of alkali type on the phase and shape of the products was also investigated, as shown in Fig. 6 (a)-(d). As mentioned above, cubic BFO crystals and amorphous  $\text{Fe}(\text{OH})_3$  nanoparticles coexist in the initial precipitation when NaOH is used as mineralizer (Fig. 6b). However, tetragonal  $\text{Bi}_2\text{O}_2\text{CO}_3$  crystals (space group:  $I4/mmm$ ) and some amorphous phases are obtained when NaOH is substituted with the same amount of KOH (Fig. 6a). It is inferred that the carbon element in  $\text{Bi}_2\text{O}_2\text{CO}_3$  can only come from the atmosphere. After the initial precipitations are both hydrothermally treated at 180 °C for 24 h, BFO cuboids are synthesized with NaOH while a mixture of spherical  $\text{BiFeO}_3$  and hexagon-like  $\alpha\text{-Fe}_2\text{O}_3$  is obtained with KOH, as shown in Fig. 6 (c), (d). Effects of alkali ions including  $\text{Li}^+$ ,  $\text{Na}^+$  and  $\text{K}^+$  on the

phase structure, morphology and size of rare earth fluoride or bismuth ferrite ( $\text{BiFeO}_3$ ) obtained by hydrothermal process have been investigated systematically.<sup>37, 38</sup> It is reported that the particle size of  $\text{BiFeO}_3$  decreases following the diminution of cationic radii ( $\text{Na}^+=1.32 \text{ \AA} < \text{K}^+=1.78 \text{ \AA}$ ). Similarly, the dimension of  $\text{BiFeO}_3$  and  $\text{Fe}_2\text{O}_3$  obtained in concentrated KOH is around 10  $\mu\text{m}$  which is much larger than that of  $\text{Bi}_2\text{Fe}_4\text{O}_9$  (around 3  $\mu\text{m}$ ) prepared with NaOH. Therefore, the cations, such as  $\text{Na}^+$  and  $\text{K}^+$ , also play a key role in the initial chemical reaction and the following crystal growth process which finally alters the phase structure and the morphology of the final products.



**Fig. 6.** XRD patterns and SEM images of the products synthesized at 180 °C for 0 h with KOH (a), NaOH (b) and for 24 h with KOH (c), NaOH. The amount of substance of NaOH and KOH are equal here.

Fig. 7 shows the UV-Vis-NIR absorption spectrum of S-24h. In general, single-phase oxide semiconductors have only one absorption edge which is usually attributed to interband transition, that's why UV-Vis spectrum can be used to evaluate the value of the band gap.<sup>6, 39, 40</sup> However, different from conventional oxide semiconductors, such as  $\text{BiFeO}_3$ ,  $\text{BiVO}_4$ ,  $\alpha\text{-Fe}_2\text{O}_3$ , and  $\text{Bi}_2\text{WO}_6$ ,<sup>6, 39-41</sup> BFO crystals possess two evident absorption edges in the visible light range, one is at about 610 nm and the other one is at about 850 nm, which are similar to the previously reported results.<sup>19, 42, 43</sup> As shown in Fig. 8, BFO contains nonequivalent edge-sharing  $[\text{FeO}_6]^{9-}$  octahedron chains and corner-sharing  $[\text{FeO}_4]^{5-}$  tetrahedron pairs. According to the crystal field theory (CFT), the 3d orbitals of both  $\text{Fe}^{3+}$  and  $\text{Fe}^{2+}$  will split into a threefold degenerate  $t_{2g}$  orbital and a double degenerate  $e_g$  orbital due to the static electric field produced by their surrounding O ligands. The energy of  $t_{2g}$  orbital is lower than that of  $e_g$  orbital in the octahedral symmetry but will get inverted in the tetrahedral symmetry, as shown in Fig. S9.<sup>44</sup> Besides, all the 3d electrons of  $\text{Fe}^{3+}$  or  $\text{Fe}^{2+}$  should occupy the 3d orbitals singly on account of the weak-field of  $\text{O}^{2-}$  ligand, which means high spin state and strong electronic correlations on Fe site. It is also well accepted that UV-Vis absorption of an oxide semiconductor is primarily originated from the superposition of transitions involving ligand field transition (intra-atomic transition), charge transfer transition (interatomic transition), and interband transition. Based on the Ab initio calculation, a narrow middle band consist of Fe  $t_{2g}$  (O)/ Fe  $e_g$  (T) orbitals and a conduction band composed of Fe  $e_g$  (O)/ Fe  $t_{2g}$  (T) orbitals were proposed by former workers.<sup>19</sup> Thus the second absorption edge was ascribed to the d-d transition between the narrow middle band Fe  $t_{2g}$  (O)/ Fe  $e_g$  (T) and the conduction band Fe  $e_g$  (O)/ Fe  $t_{2g}$  (T). However, the origin of the second absorption edge is quite controversial because d-d transition belongs to an intra-atomic transition rather than an inter-

band transition. Moreover, Pchelkina et al. derived an asymmetric DOS in BFO and a single bandgap varies from 0.97eV to 1.28eV based on their Ab initio investigation. Moreover, the up-spin and down-spin branches in their calculated DOS should be asymmetric rather than symmetric owing to the high spin state of  $\text{Fe}^{3+}$ . Pchelkina et al. not only derived an asymmetric DOS in BFO but also a single bandgap varies from 0.97eV to 1.28eV based on their first principle calculation.<sup>20</sup> Besides, a calculated middle band composed of Fe  $t_{2g}$  (O)/ Fe  $e_g$  (T) was also obtained in  $\text{KBiFe}_2\text{O}_5$  semiconductor which had only one absorption edge indicating the extra absorption edge was not caused by the calculated narrow middle band.<sup>44</sup> In principle, the d-d transition here is both spin and laporte forbidden according to the spectroscopic selection rules. The molar absorption coefficient of the ligand field transition in  $\text{Fe}^{3+}$  with high spin state is about three orders of magnitude lower than that of charge transfer transition.<sup>45</sup> Although crystal field distortion and hybridization of Fe 3d and O 2p orbitals could relax the spin and laporte forbidden transition to some extent.<sup>46</sup> The probability of ligand field transition is still extremely limited. As a result, the extra strong absorption edge at 850 nm should not result from d-d transition as reported. It has been investigated that  $\text{Fe}_3\text{O}_4$  crystals show intensive absorption throughout the whole UV-Vis range owing to the intervalence charge transfer (IVCT) between randomly arranged  $\text{Fe}^{2+}$  and  $\text{Fe}^{3+}$ .<sup>47</sup> In BFO crystals, the octahedral  $[\text{FeO}_6]^{9-}$  chain are connected by isolated tetrahedral  $[\text{FeO}_4]^{5-}$  pairs with all  $\text{Bi}^{3+}$  occupying equivalent sites. The uneven distributed negative charges tend to induce variation in valence state of  $\text{Fe}^{3+}$  and a certain amount of  $\text{Fe}^{2+}$  in BFO crystals is demonstrated via XPS, as presented in Fig. 9. The  $2p_{3/2}$  binding energies of the  $\text{Fe}^{2+}$  and  $\text{Fe}^{3+}$  were reported at 709.5 eV and 710.9 eV, respectively.<sup>48</sup> However, the Fe  $2p_{3/2}$  binding energy in the obtained XPS spectrum located at  $\sim 710.1\text{eV}$  indicating the coexistence of  $\text{Fe}^{2+}$  and  $\text{Fe}^{3+}$ , which coincide

with a previous study on BFO.<sup>49</sup> The ratio of Fe<sup>2+</sup>: Fe<sup>3+</sup> is estimated to be 39:61 using the Lorentzian fitting method. Therefore, similar to Fe<sub>3</sub>O<sub>4</sub>, IVCT without restriction of selection rule is also likely to happen in BFO crystals and brings about intense interatomic

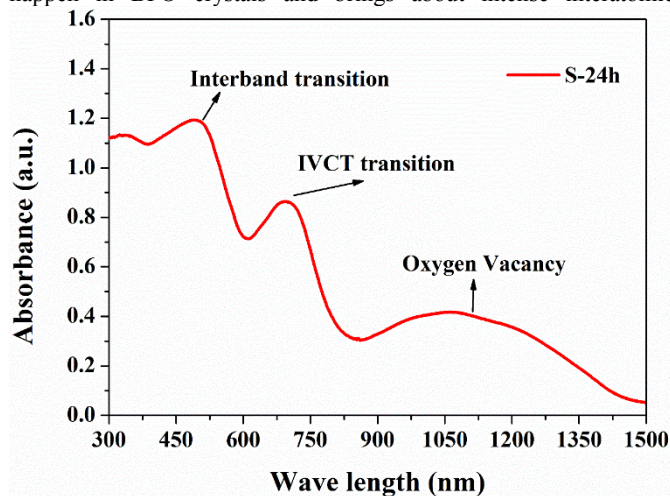


**Fig. 7** UV-visible and near infrared absorption spectrum of S-24h. The absorption peak at around 500 nm belongs to interband transition, the extra absorption peak at about 700 nm is caused by intervalence charge transfer (IVCT) transition and the broad absorption peak at 1100 nm is result from abundant oxygen vacancy.

absorption. However, different from IVCT in Fe<sub>3</sub>O<sub>4</sub>, IVCT in BFO is localized due to the isolated [FeO<sub>4</sub>]<sup>5-</sup> pair and thus results in a charge-transfer insulator.<sup>50</sup>

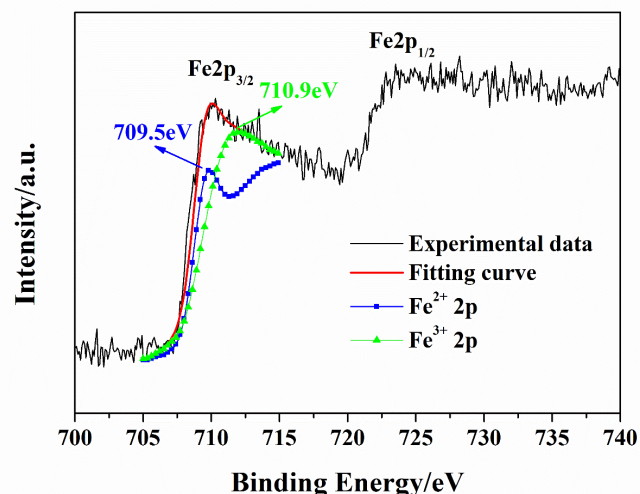


**Fig. 9** High resolution X-ray photoelectron spectrum of the Fe 2p peaks for BFO cuboids. The overlapped Fe 2p peak at 710.1 eV is fitted by Fe<sup>2+</sup> 2p<sub>3/2</sub> at 709.5 eV and Fe<sup>3+</sup> 2p<sub>3/2</sub> at 710.9 eV using Lorentzian fitting method.

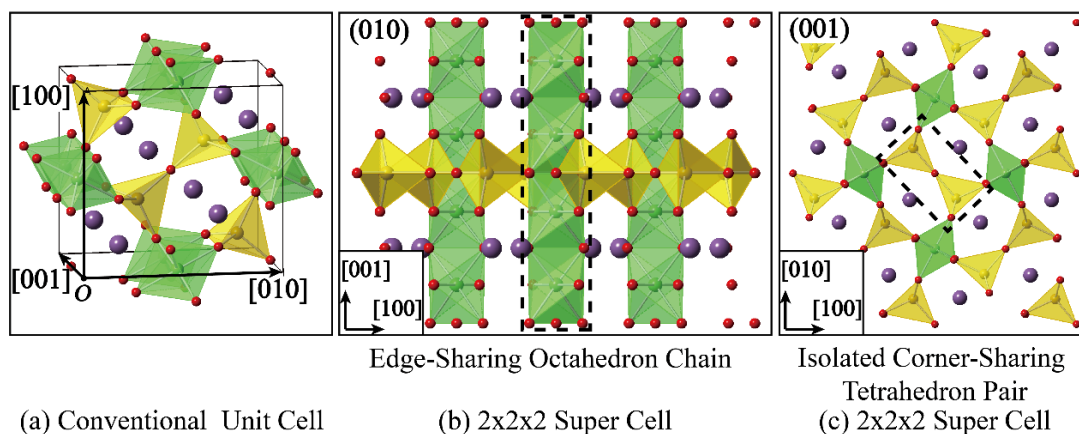


**Fig. 8** Schematic illustration of the conventional unit cell of BFO crystal (a) and side view along [010] (b), [001] (c) directions of the 2x2x2 super cell. The edge-sharing [FeO<sub>6</sub>]<sup>-9</sup> octahedron chains are connected by isolated [FeO<sub>4</sub>]<sup>-5</sup> corner-sharing tetrahedron pairs.

In addition, it is important to note that BFO crystals not only have very broad absorption in the UV-Vis light range, but also possess remarkable absorption to NIR light compared with other reported semiconductors including the hottest perovskite sensitizer CH<sub>3</sub>NH<sub>3</sub>PbI<sub>3</sub>.<sup>4, 5, 44</sup> The significant NIR absorption is attributed to oxygen vacancies produced by the existence of Fe<sup>2+</sup> which is similar with W<sub>18</sub>O<sub>49</sub> and Bi<sub>2</sub>WO<sub>6</sub> nanosheets.<sup>5, 51</sup> This result is of significance in fully utilizing the solar energy and exploring potential applications in NIR related fields. In addition, the existence of oxygen vacancies also indicate that Bi<sub>2</sub>Fe<sub>4</sub>O<sub>9</sub> is an n-type oxide semiconductor as with other most widely studied oxide semiconductors.

The band gap of BFO cuboids can be determined by the following Tauc's relation using data of UV-Vis-NIR diffuse reflectance spectra:

$$ah\nu = A(h\nu - E_g)^{n/2} \quad (8)$$

where  $h$ ,  $\nu$ ,  $A$ ,  $E_g$  and  $\alpha$  stand for Planck's constant, light frequency, absorbance constant, band gap and absorption coefficient, respectively. In the equation,  $n=1$  decides a direct transition while  $n=4$  decides an indirect transition. Up to now, BFO was often regarded as a direct band gap semiconductor with an intrinsic band gap of ~2 eV. However, our first-principle calculation clearly indicates that BFO should be an indirect band gap semiconductor because the valence-band maximum ( $E_v$ ) and the conduction-band minimum ( $E_c$ ) locate at different k-points, as shown in Fig. 10. The calculated band gap is 1.23 eV. The band gap derived by plotting  $(ah\nu)^{1/2}$  versus the photon energy  $h\nu$  near the interband absorption edge is 1.29 eV when considering BFO as an indirect semiconductor (Fig. 11). This value is lower than the values (2.05 eV, 1.53 eV) derived from taking BFO

as a direct bandgap semiconductor,<sup>12</sup> but is well consistent with our calculated value. It is interesting to note that all the double degenerated orbitals will split into two single orbitals between the G

(0,0,0,0) point and the T(-0.5,0,0,0.5) point (Fig. 10) which is probably owing to the strong electronic interaction and the unique arrangement of tetrahedron and octahedron units.

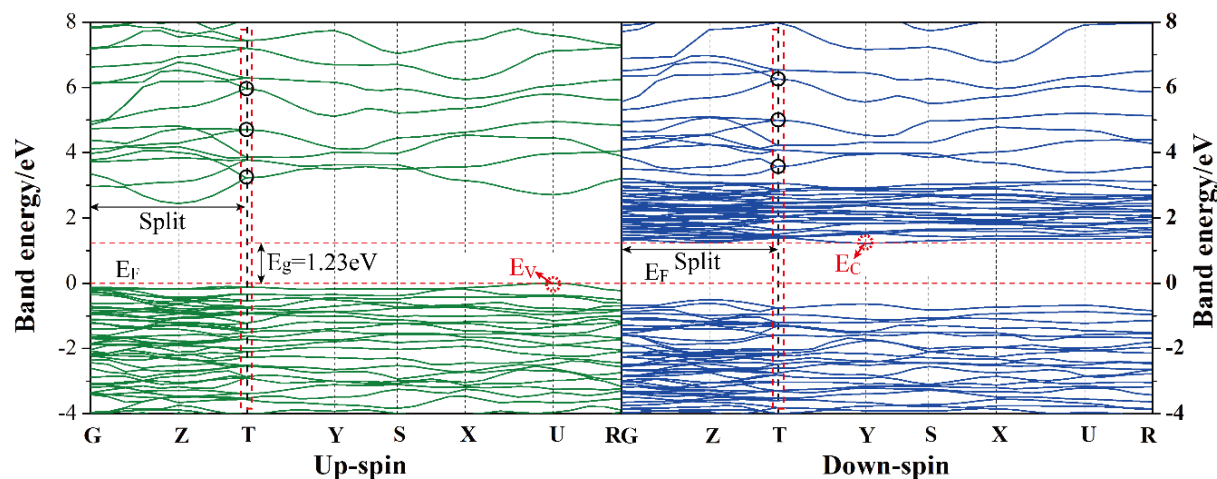


Fig. 10 Calculated band structure for BFO crystals along the high-symmetry axes of the Brillouin zone.

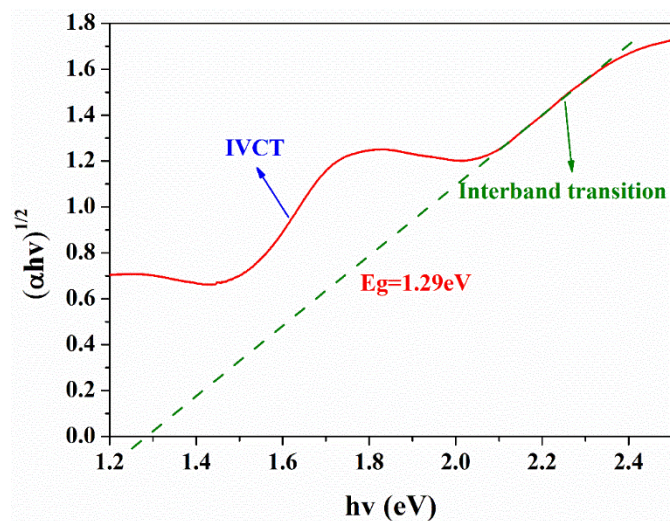


Fig. 11 Plots of  $(\alpha hv)^{1/2}$  versus photon energy  $h\nu$  around the absorption edges of S-24h.

The total and partial density of states (DOS) of BFO with up-spin and down-spin components are also calculated to clarify the feature of the interband transition in BFO, as displayed in Fig. 12. The up-spin and down-spin branch are asymmetric owing to the high spin state of  $\text{Fe}^{3+}$  which is in good agreement with the other reported result.<sup>20</sup> The top of the valence band is mainly dominated by the O 2p states, while the bottom of the conduction band is defined by Fe 3d states. Thus the interband transition is mainly contributed by O 2p to Fe 3d transition.

Despite of the narrow band gap and strong absorption in Vis-NIR range, the photoelectrochemical properties of BFO, especially under NIR irradiation, are seldom investigated. The time-dependent photocurrent for BFO cuboids with chopped visible-light and UV-visible-light irradiation are shown in Fig. 13. The photocurrent density is  $7 \mu\text{A cm}^{-2}$  under visible light while the value nearly quintupled, as large as  $33 \mu\text{A cm}^{-2}$  when exposed to UV-visible light. The photoelectric responses are found to be much more sensitive and the photocurrents are more stable compared with previously reported

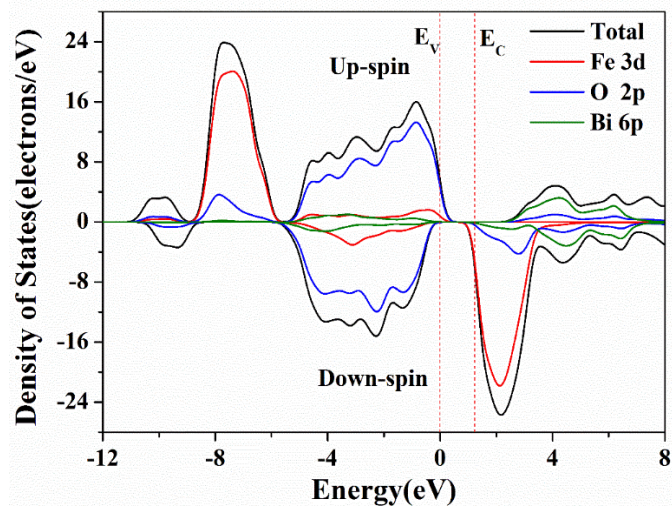
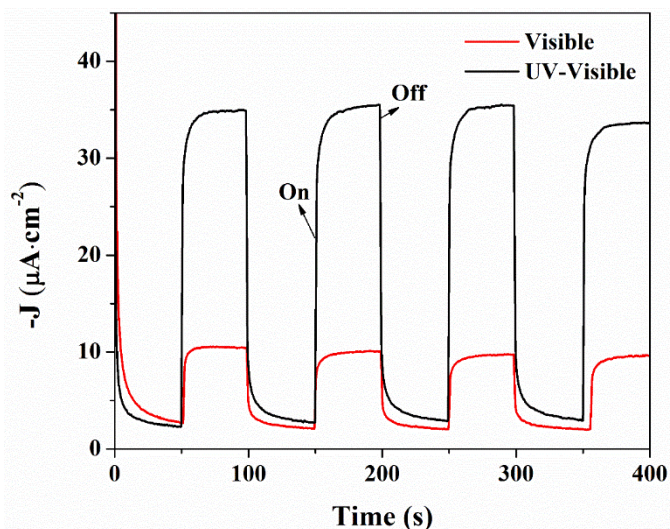


Fig. 12 Up-spin (upper branch) and down-spin (lower branch) components of total density of states (DOS) and partial DOS of BFO crystals.

results implying a more efficient charge transfer in DB-BFO film electrode which was probably brought about by the orientation of BFO cuboids.<sup>12</sup> Small but distinct photoelectric response of BFO cuboids under chopped NIR irradiation ( $\lambda > 780 \text{ nm}$ ) is measured and the photocurrent is around  $0.35 \mu\text{A cm}^{-2}$ , as shown in Fig. 14. It has been investigated in Fig. 7 that the NIR absorption in BFO is much lower than visible light absorption and electrolyte solution between the BFO photoanode and the solar light simulator can also absorb a big part of NIR irradiation while UV-Vis light is barely weakened, which both lead to a small photocurrent.<sup>53</sup> Despite of the low photocurrent, the PEC measurement of BFO under NIR irradiation intuitively proved its ability to utilizing NIR irradiation. In theory, sufficient over-potentials of both the valence band edge (VBE) and the conduction band edge (CBE) versus  $E_{\text{O}_2/\text{H}_2\text{O}} = +1.229 \text{ V}$  (vs. SHE, 298 K) and  $E_{\text{H}^+/\text{H}_2} = 0 \text{ V}$  (vs. SHE, 298 K) are essential for an ideal semiconductor used in a photoelectrochemical cell.<sup>45, 54</sup> The optical band gap of BFO (1.29 eV) is very close to the potential difference

between  $E_{O_2/H_2O}$  and  $E_{H^+/H_2}$  implying insufficient over-potentials in single-phase BFO. Therefore, the photoelectrochemical performance of BFO cuboid was not as good as the well-studied  $BiVO_4$  ( $E_g=2.4$  eV).<sup>55</sup> Accounting for its low bandgap and the UV-Vis-NIR all band absorption feature, photoanodes based on BFO should have potential

applications in water photocatalytic splitting and toxic organic pollutants degradation. More importantly, the evident NIR absorption of BFO crystal can encourage people to study its applications in other NIR light related fields.



**Fig. 13** Time-dependent photocurrents of the BFO cuboids film electrode under on-off visible ( $\lambda > 420$  nm) and UV-visible exposure in 0.1 M  $K_3PO_4$ , respectively, with a constant bias of +0.7 V vs SCE. Experiments were performed using back illumination and pH=7 electrolyte.

## Conclusion

In summary, single-phase mono-dispersed BFO cuboids have been synthesized successfully using a cost-effective and practical low temperature hydrothermal method in concentrated NaOH solution. The formation of the BFO crystal is based on the reaction between  $Bi_{25}FeO_{40}$  crystal and amorphous  $Fe(OH)_3$  and the cuboid shape is resulted from the “blocking effect” of concentrated  $OH^-$ . The BFO cuboid is preferentially grown along [001] direction and its dominating facets are (001), (110) and  $(\bar{1}10)$ . The cuboid-shaped BFO crystals is an n-type oxide semiconductor that not only exhibit broad and intensive absorption in all UV-Vis light range but also show very strong NIR absorption suggesting an ability to make use of a broader range of the solar light spectrum including a considerable part of the NIR irradiation and potential applications in fields related to NIR light. Therefore, steady and distinct photocurrents that have rapid response to irradiation are measured to be  $0.35 \mu A cm^{-2}$ ,  $7 \mu A cm^{-2}$  and  $33 \mu A cm^{-2}$  under chopped NIR irradiation, visible light and UV-Vis light, respectively. First principle calculation reveals that BFO is an indirect semiconductor with a band gap of 1.23 eV which is comparable with the experimental value 1.29 eV. In addition, the origin of the extra absorption peak at around 700 nm in the UV-Vis-NIR spectrum should be attributed to the IVCT induced by an unevenly distribution of  $[FeO_6]^{9-}$  octahedrons and  $[FeO_4]^{5-}$  tetrahedrons rather than the d-d transition.

## Acknowledgement

This work is supported by the Natural Science Foundation of China

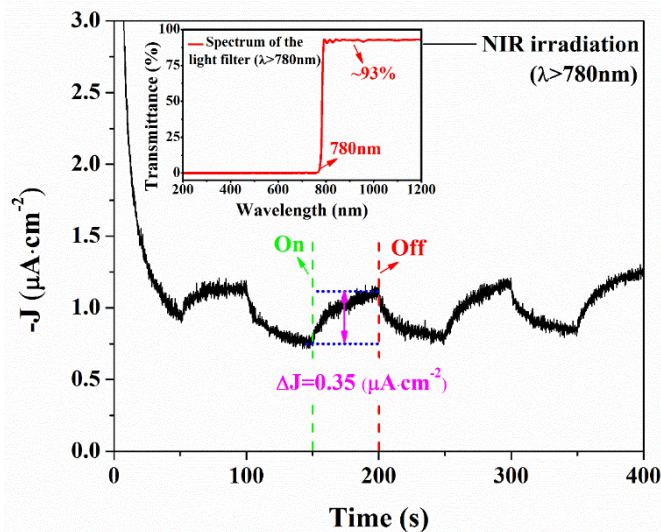


**Fig. 14** Time-dependent photocurrent of the BFO cuboids film electrode under on-off near-infrared (NIR) irradiation ( $\lambda > 780$  nm) in 0.1 M  $K_3PO_4$  with a constant bias of +0.7 V vs SCE. The inset shows the reflectance spectrum of the light filter. In order to eliminate the interference of the NIR irradiation from the environment, the experiment were performed in pH=7 electrolyte surrounded by ice cubes at night using back illumination.

(No. 11074165 and No. 11304198). Instrumental Analysis Center of Shanghai Jiao Tong University and National Engineering Research Center for Nanotechnology were sincerely acknowledged for assisting relevant analyses.

## Notes and references

State Key Laboratory of Metal Matrix Composites, School of Materials Science and Engineering, Shanghai Jiaotong University, Shanghai 200240, People's Republic of China.

Corresponding author: Yiping Guo, ypguo@sjtu.edu.cn; Hezhou Liu, hzhliu@sjtu.edu.cn; Tel.: +86 021 34202549.

- 1 S. U. Khan, M. Al-Shahry, and W. B. Ingler, *Science*, 2002, **297**, 2243.
- 2 D. Chen, and J. Ye, *Adv. Funct. Mater.*, 2008, **18**, 1922.
- 3 F. Lu, W. Cai, and Y. Zhang, *Adv. Funct. Mater.*, 2008, **18**, 1047.
- 4 G. Xing, N. Mathews, S. Sun, S. S. Lim, Y. M. Lam, M. Grätzel, S. Mhaisalkar, and T. C. Sum, *Science*, 2013, **342**, 344.
- 5 J. Tian, Y. Sang, G. Yu, H. Jiang, X. Mu, and H. Liu, *Adv. Mater.*, 2013, **25**, 5075.
- 6 F. Gao, X. Chen, K. Yin, S. Dong, Z. Ren, F. Yuan, T. Yu, Z. Zou, and J. M. Liu, *Adv. Mater.*, 2007, **19**, 2889.
- 7 G. Catalan, and J. F. Scott, *Adv. Mater.*, 2009, **21**, 2463.
- 8 T. Choi, S. Lee, Y. Choi, V. Kiryukhin, and S.-W. Cheong, *Science*, 2009, **324**, 63.
- 9 Q. J. Ruan, and W. D. Zhang, *J. Phys. Chem. C*, 2009, **113**, 4168.
- 10 A. Poghossian, H. Abovian, P. Avakian, S. Mkrtchian, and V. Haroutunian, *Sens. Actuators, B*, 1991, **4**, 545.

- 11 N. Zakharchenko, *Kinet. Catal.*, 2002, **43**, 95.
- 12 Y. Li, Y. Zhang, W. Ye, J. Yu, C. Lu, and L. Xia, *New J. Chem.*, 2012, **36**, 1297.
- 13 H. Koizumi, N. Niizeki, and T. Ikeda, *Jpn. J. Appl. Phys.*, 1964, **3**, 495.
- 14 Z. Yang, Y. Huang, B. Dong, H. L. Li, and S. Q. Shi, *J. Solid State Chem.*, 2006, **179**, 3324.
- 15 T.-J. Park, G. C. Papaefthymiou, A. R. Moodenbaugh, Y. Mao, and S. S. Wong, *J. Mater. Chem.*, 2005, **15**, 2099.
- 16 J. T. Han, Y. H. Huang, R. J. Jia, G. C. Shan, R. Q. Guo, and W. Huang, *J. Cryst. Growth*, 2006, **294**, 469.
- 17 A. Maitre, M. Francois, and J. Gachon, *J. Phase Equilib. Diff.*, 2004, **25**, 59.
- 18 X. Zhang, L. Bourgeois, J. Yao, H. Wang, and P. A. Webley, *Small*, 2007, **3**, 1523.
- 19 S. Sun, W. Wang, L. Zhang, and M. Shang, *J. Phys. Chem. C*, 2009, **113**, 12826.
- 20 Z. Pchelkina, and S. Streltsov, *Physical Review B*, 2013, **88**, 054424.
- 21 F. Wooten, *Optical properties of solids*. Vol. 111. 1972: Academic Press: New York.
- 22 V. Dolocan, and F. Iova, *Phys. Status Solidi A*, 1981, **64**, 755.
- 23 C. Wang, and B. Klein, *Phys. Rev. B*, 1981, **24**, 3393.
- 24 J. Neaton, C. Ederer, U. Waghmare, N. Spaldin, and K. Rabe, *Physical Review B*, 2005, **71**, 014113.
- 25 J. P. Perdew, K. Burke, and M. Ernzerhof, *Phys. Rev. Lett.*, 1996, **77**, 3865.
- 26 P. E. Blöchl, *Phys. Rev. B*, 1994, **50**, 17953.
- 27 N. Shamir, E. Gurewitz, and H. Shaked, *Acta Crystallogr., Sect. A: Found. Crystallogr.*, 1978, **34**, 662.
- 28 V. I. Anisimov, F. Aryasetiawan, and A. Lichtenstein, *J. Phys. - Condens. Mat.*, 1997, **9**, 767.
- 29 H. J. Monkhorst, and J. D. Pack, *Phys. Rev. B*, 1976, **13**, 5188.
- 30 S. Radaev, L. Muradyan, and V. Simonov, *Acta Crystallogr., Sect. B: Struct. Sci.*, 1991, **47**, 1.
- 31 P. Patnaik, *Dean's analytical chemistry handbook*. Vol. 1143. 2004: McGraw-Hill: New York.
- 32 C. Chen, J. Cheng, S. Yu, L. Che, and Z. Meng, *J. Cryst. Growth*, 2006, **291**, 135.
- 33 S. H. Han, K. S. Kim, H. G. Kim, H. G. Lee, H. W. Kang, J. S. Kim, and C. I. Cheon, *Ceram. Int.*, 2010, **36**, 1365.
- 34 N. Niizeki, and M. Wachi, *Z. Krist. -New Cryst. St.*, 1968, **127**, 173.
- 35 J. Zhang, Z. Lin, Y. Lan, G. Ren, D. Chen, F. Huang, and M. Hong, *JACS*, 2006, **128**, 12981.
- 36 Y. Chang, and H. C. Zeng, *Cryst. Growth Des.*, 2004, **4**, 273.
- 37 X. Xue, L. Wang, L. Huang, D. Zhao, and W. Qin, *CrystEngComm*, 2013, **15**, 2897.
- 38 M. Hojamberdiev, Y. Xu, F. Wang, J. Wang, W. Liu, and M. Wang, *Ceramics-Silikáty*, 2009, **53**, 113.
- 39 L. Ren, L. Jin, J. B. Wang, F. Yang, M. Q. Qiu, and Y. Yu, *Nanotechnology*, 2009, **20**, 115603.
- 40 L. W. Zhang, Y. J. Wang, H. Y. Cheng, W. Q. Yao, and Y. F. Zhu, *Adv. Mater.*, 2009, **21**, 1286.
- 41 S. Mitra, S. Das, K. Mandal, and S. Chaudhuri, *Nanotechnology*, 2007, **18**, 275608.
- 42 Y. Liu, and R. Zuo, *Particuology*, 2012, **11**, 581.
- 43 Q. Zhang, W. Gong, J. Wang, X. Ning, Z. Wang, X. Zhao, W. Ren, and Z. Zhang, *J. Phys. Chem. C*, 2011, **115**, 25241.
- 44 G. Zhang, H. Wu, G. Li, Q. Huang, C. Yang, F. Huang, F. Liao, and J. Lin, *Sci. Rep.*, 2013, **3**, 1265.
- 45 F. A. Cotton, G. Wilkinson, C. A. Murillo, and M. Bochmann, *Advanced inorganic chemistry*. Vol. 5. 1988: Wiley: New York.
- 46 Y. He, Y. Miao, C. Li, S. Wang, L. Cao, S. Xie, G. Yang, B. Zou, and C. Burda, *Phys. Rev. B*, 2005, **71**, 125411.
- 47 W. Fontijn, P. Van der Zaag, L. Feiner, R. Metselaar, and M. Devillers, *J. Appl. Phys.*, 1999, **85**, 5100.
- 48 T. Schedel-Niedrig, W. Weiss, and R. Schlögl, *Physical Review B*, 1995, **52**, 17449.
- 49 Z. Tian, Y. Qiu, S. Yuan, M. Wu, S. Huo, and H. Duan, *J. Appl. Phys.*, 2010, **108**, 064110.
- 50 J. Zaanen, G. Sawatzky, and J. Allen, *Phys. Rev. Lett.*, 1985, **55**, 418.
- 51 G. Leftheriotis, S. Papaefthimiou, P. Yianoulis, and A. Siokou, *Thin Solid Films*, 2001, **384**, 298.
- 52 P. Kubelka, and F. Munk, *Z. Tech. Phys.*, 1931, **12**, 593.
- 53 B. Wozniak, and J. Dera, *Light absorption in sea water*. Vol. 33. 2007: Springer: New York.
- 54 K. J. McDonald, and K. S. Choi, *Chem. Mater.*, 2011, **23**, 4863.
- 55 S. P. Berglund, D. W. Flaherty, N. T. Hahn, A. J. Bard, and C. B. Mullins, *J. Phys. Chem. C*, 2011, **115**, 3794.

**Graphical Abstract:**

The [001]-oriented cuboid-shaped  $\text{Bi}_2\text{Fe}_4\text{O}_9$  with an indirect bandgap of 1.29 eV and strong absorption in all solar spectrum shows distinct photocurrent as photoanode.

